Secondary-Side Voltage Control via Primary-Side Controller for Wireless EV Chargers

NATTAPONG HATCHAVANICH, (Member, IEEE), ANAWACH SANGSWANG, (Member, IEEE), AND MONGKOL KONGHIRUN, (Senior Member, IEEE)
Department of Electrical Engineering, Faculty of Engineering, King Mongkut's University of Technology Thonburi, Bangkok 10140, Thailand

Corresponding author: Anawach Sangswang (anawach.san@kmutt.ac.th)

ABSTRACT In inductive power transfer (IPT) system, the magnetic coupling has significant effects on power and system efficiency. The voltage and current on the secondary side are coupling dependent. Load measurements are not possible through sensors on the primary side. This article proposes the secondary-side voltage controller based on the primary-side control by means of bifurcation approach. The main advantage of operation under bifurcation is that the coupling and load on the secondary have no effect on the voltage gain. This enables the secondary voltage control through the primary voltage. With the proposed sensing coil on the primary side, the bifurcation detection is possible. The proposed control can utilize the frequency split phenomenon and track the bifurcation frequency to ensure maximum efficiency in various coupling conditions. In addition, the design guidelines of the parallel-parallel compensation configuration are introduced for a desired load profile and transfer distance. The constant voltage gain with respect to conditions of magnetic coupling variation is verified by using finite element analysis and experimental study. A 1-kW IPT prototype is constructed to validate the proposed bifurcation detection and voltage control. Experimental results show that the proposed IPT can achieve up to 90% of maximum efficiency while maintaining constant secondary voltage.

INDEX TERMS Bifurcation, inductive power transfer, sensing coil.

I. INTRODUCTION

An inductive power transfer (IPT) based wireless charger offers several benefits such as electrical and mechanical safety isolation, safe operation in harsh environment, and fully automatic charging procedure for electric vehicles (EVs), comparing with conventional plug-in chargers [1]. In fact, the circuit configuration of an IPT based wireless charger is similar to a traditional plug-in charger. The AC-DC converter regulates the dc-bus voltage for the resonant inverter. The resonant inverter then supplies high alternating voltage or current to the loosely air-core coupled coils separated by large air gap, causing considerable leakage flux.

A reactive power compensation is commonly chosen to overcome the issue of poor magnetic coupling. Commonly used topologies are series-series (SS), series-parallel (SP), parallel-series (PS) and parallel-parallel (PP) compensations.

The associate editor coordinating the review of this manuscript and approving it for publication was Kai Song.

The two weakly coupled resonant networks are tuned to the resonant frequency ω_0 to provide the zero-phase-angle frequency (ZPA). Parameter variations cause a split in the resonant frequency ω_0 into multiple ZPA frequencies. The instability of the number of ZPA frequencies is known as bifurcation in IPT [2]. The SS topology is the only topology that achieves the independence feature between operating frequency and magnetic coupling variations. The reflected reactance is always equal to zero on the primary side [3].

The power control strategies are used to regulate the primary voltage based on the primary side controller. The control methods in past work are based on modifications of switching sequence of the inverter. The asymmetrical voltage cancellation (AVC) [4] and symmetrical voltage cancellation (SVC) [5], [6] can be used in full-bridge topologies. The single-stage boost bridgeless converter offering power factor correction (PFC) for high power, high efficiency, and high power factor is reported in [7]. Unfortunately, it can be operated only in a fixed or narrow frequency range. In [8], [9],

the phase shifting method is proposed to address the load variations under practical operation.

However, the mentioned control strategies simply do not work under bifurcation due to the instability of the ZPA frequency. The phase-lock-loop (PLL) control has been used to track the ZPA of the input impedance [10]. The bifurcation phenomenon results in an increased number of ZPA frequencies and the frequency tracking becomes a formidable task. In [11], the ZPA detection using the inverter output voltage and the secondary current is reported to solve the problem of multiple ZPA frequencies under bifurcation. However, the communication between primary and secondary subsystems has further complicated the system.

Under bifurcation, the original resonant frequency no longer supplies the maximum power [12]. In [13], an intermediate coil is added to form a three-coil configuration for the single boosting effect, an increased apparent coupling coefficient, which in turns induces the bifurcation phenomenon. The output voltage (V_o) can be estimated while high transfer efficiency is achieved. In [14], the four-coil series resonator with two intermediate coils located in the primary side offers double boosting effect for further increased coupling coefficient. Theoretically, the voltage gain can be unity and the RMS input current can be reduced, compared with [13]. However, under misalignment conditions, the majority of the induced effect occurs on the intermediate coil as opposed to the secondary coil. The coupling coefficient is greatly reduced causing an excessive circulating current in the primary side.

In fact, the bifurcation can be avoided or allowed as needed, by either adopting complicated control strategies or proper design considerations. The primary and secondary quality factors (Q) are used in the bifurcation criteria through the discriminant of the input reactance [2]. Initially, most WPT systems are designed to avoid the bifurcated region because a sudden change of impedance characteristics after the bifurcation boundary is undesirable. Recent research efforts have been directed toward investigating the benefits of operation under bifurcation. The critical coupling (k_{cri}) has been adopted as the bifurcation boundary. Table 1 summarizes the reported bifurcation criteria [15]–[19]

Clearly, the bifurcation determination requires an exact value of the coupling k. Various sensors including infrared sensors, tunneling magnetoresistive (TMR) and sensing coils are used to detect the position of the secondary coils [20]–[23]. In practice, the exact determination of the coupling k remains rather difficult.

Although the bifurcation can provide high constant output current in SS compensation system, the output voltage level is not suitable for the on-board charger. The PP compensation, on the other hand, provides higher secondary voltage under bifurcation. In [19], the non-ZVS region due to bifurcation can be avoided by a given design procedure to operate at the original resonant frequency. The differences between this work and what was done in [19] are as follows.

TABLE 1. Bifurcation criteria in literature.

Ref.	Year	Circuit Topology	No. of Coils	Bifurcation	Bifurcation Criteria
[2]	2004	SS	2	Avoid	$Q_1 > \dfrac{4Q_2^3}{4Q_2^2 - 1}$
		SP & PP			$Q_1 > Q_2 + \dfrac{1}{Q_2}$
		PS			$Q_1 > Q_2$
[15]	2011	SS	4	Allow	$k_{cri} > 1/Q_{coil}$
[16]	2015	SS	2 & 4	Allow	
[17]	2016	SS	2	Allow	$k_{cri} > \dfrac{1}{Q_2}\sqrt{1 - \dfrac{1}{4Q_2^2}}$
[18]	2019	SS	2	Allow	$k_{cri} > \sqrt{\dfrac{1}{Q_1 Q_2}}$
[19]	2019	SS	2	Avoid	$k_{cri} < \dfrac{1}{Q_2}\sqrt{1 - \dfrac{1}{4Q_2^2}}$

*Q_1 and Q_2 are primary and secondary quality factors, respectively.
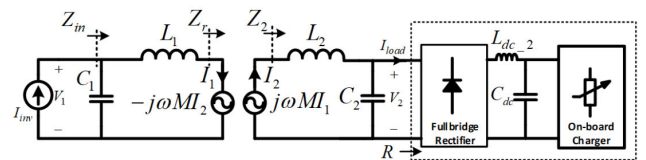

FIGURE 1. Equivalent circuit of PP compensation.

- The operating region in this work is intended to be under bifurcated condition as opposed to avoiding it. Therefore, a bifurcation detection is proposed with a sensing coil.
- No sensor is needed on the secondary side, since the secondary voltage and current can be estimated from the primary side.

In this article, the PP configuration with a full-bridge current-source inverter (CSI) is adopted. The output voltage is targeted at a compatible voltage level of the on-board charger. The constant output voltage operation under flexible charging distances can be accomplished. The bifurcation phenomenon is observed by an additional sensing coil installed at the primary side. With the proposed designed procedure, the constant voltages on both sides can be achieved while providing a flexibility on the coil positions.

II. PRINCIPLE OF PP COMPENSATION
An equivalent circuit focusing on the PP compensation is shown in Figure 1. The compensation circuits are commonly tuned at the same resonant frequency. Both sides are magnetically coupled with the coupling coefficient k_{12} described as,

$$k_{12} = M_{12}/\sqrt{L_1 L_2} \tag{1}$$

The impedance of the secondary circuit (Z_2) is given by,

$$Z_2 = j\omega L_2 + \frac{1}{j\omega C_2 + (1/R)} \tag{2}$$

The reflected impedance (Z_r) from the secondary side referred to the primary side is given as,

$$Z_r = \frac{\omega^2 k_{12}^2 L_1 L_2}{Z_2} \tag{3}$$

The reflected resistance and reactance are expressed as,

$$\text{Re}\{Z_r\} = \frac{\omega^2 k_{12}^2 L_1 L_2 R}{R^2 \left(\omega^2 C_2 L_2 - 1\right)^2 + \omega^2 L_2^2}, \tag{4}$$

and

$$\text{Im}\{Z_r\} = \frac{-\omega^3 k_{12}^2 L_1 L_2 \left[C_2 R^2 \left(\omega^2 L_2 C_2 - 1\right) + L_2\right]}{R^2 \left(\omega^2 C_2 L_2 - 1\right)^2 + \omega^2 L_2^2}, \tag{5}$$

respectively. The primary and secondary sides are tuned at the same natural frequency. Therefore, the primary capacitance is given by,

$$C_1 = \frac{C_2 L_2}{L_1} \tag{6}$$

The input impedance (Z_{in}) can be calculated in (7), as shown at the bottom of the page, which can be separated into real and imaginary parts. By setting the imaginary part from (7) to zero, the ZPA frequencies can be derived as (8)–(10), as shown at the bottom of the page. The inductance L_2 is slightly changed under different coil positions. It is rather difficult to identify the coupling and load values from the primary side of the proposed setup without additional sensors or a wireless communication system. An increase in either k_{12} or R causes the bifurcation frequencies ω_1 and ω_2 to be lower and higher, respectively. Initially, the boundaries of ω_1 and ω_2 are determined using the maximum values of k_{12} and R based on the predefined operating constraints (i.e. the minimum transfer gap and the end of the charging process). In this article, the maximum ZPA frequency is set on the PLL controller to cover the frequency boundaries. The bifurcation

frequency is automatically tracked without having to evaluate the system parameters throughout the operation.

Under bifurcated condition, the conditions in (9) and (10) are met. By setting the discriminant of the input reactance ($\text{Im}\{Z_{in}\}$) in (7) to zero, the critical coupling k_{cri} is obtained by solving for k_{12} which can be given as,

$$k_{cri} = \sqrt{1 - \frac{2C_2 R^2}{L_2} - \frac{2C_2^2 R^4}{L_2^2} + \frac{2\sqrt{C_2^3 R^6 (2L_2 + C_2 R^2)}}{L_2^2}} \tag{11}$$

The critical load resistance (R_{cri}) can be obtained in the same manner,

$$R_{cri} = \sqrt{\frac{L_2}{4C_2}} \sqrt{(1 - \sqrt{1 - k_{12}^2}) \left(\frac{1 - k_{12}^2}{k_{12}^2}\right)} \tag{12}$$

By substituting (8) – (10) into (7), the impedance at the ZPA frequencies can be calculated as,

$$Z_{in}(\omega_0) = \frac{L_1 \left(1 - k_{12}^2\right)}{k_{12}^2 C_2 R} \tag{13}$$

$$Z_{in}(\omega_1) = Z_{in}(\omega_2) = \frac{L_1}{L_2} R \tag{14}$$

At the frequency ω_0, the input impedance Z_{in} depends on the vertical distance and misalignment position in terms of the coupling coefficient k_{12}. When the frequency is changed to ω_2, Z_{in} becomes independent on the coupling k_{12} as indicated in (14). In other words, the distance and misalignment no longer have effect on the input impedance and the supply voltage. The main focus of this work is on the operation at frequency ω_2.

The secondary voltage (V_2) is shown in (15), as shown at the bottom of the next page. Referring to (8) and (10),

---

$Z_{in}(j\omega)$

$$= \frac{L_1 L_2 R \omega^2 + j\omega \left(L_1 \left(R^2 + (3L_2 C_2 R^2 - L_2^2)(k_{12}^2 - 1)\omega^2 - (k_{12}^2 - 1)[C_2 L_2^3 (k_{12}^2 - 1) + 3C_2^2 L_2^2 R^2]\omega^4 - C_2 L_2^3 R^2 (k_{12}^2 - 1)\omega^6\right)\right)}{\left(R^2 + [L_2^2 - 4L_2 C_2 R^2]\omega^2 + 2[L_2(k_{12}^2 - 1) + C_2 R^2(3 - k_{12}^2)]C_2 L_2^2 \omega^4 [L_2(k_{12}^2 - 1) + 4C_2 R^2](k_{12}^2 - 1)C_2^2 L_2^3 \omega^6 + C_2^4 L_2^4 R^2 [k_{12}^2 - 1]^2 \omega^8\right)} \tag{7}$$

ω_0

$$= \frac{1}{\sqrt{L_1 C_1 \left(1 - k_{12}^2\right)}} = \frac{1}{\sqrt{L_2 C_2 \left(1 - k_{12}^2\right)}} \tag{8}$$

ω_1

$$= \sqrt{\frac{L_2 \left(1 - k_{12}^2\right) - C_2 R - \sqrt{L_2^2 \left(k_{12}^2 - 1\right) + 4C_2 R^2 \left(C_2 k_{12}^2 R^2 + L_2(k_{12}^2 - 1)\right)}}{2L_2 C_2^2 R^2 \left(k_{12}^2 - 1\right)}} \tag{9}$$

ω_2

$$= \sqrt{\frac{L_2 \left(1 - k_{12}^2\right) - C_2 R + \sqrt{L_2^2 \left(k_{12}^2 - 1\right) + 4C_2 R^2 \left(C_2 k_{12}^2 R^2 + L_2(k_{12}^2 - 1)\right)}}{2L_2 C_2^2 R^2 \left(k_{12}^2 - 1\right)}} \tag{10}$$
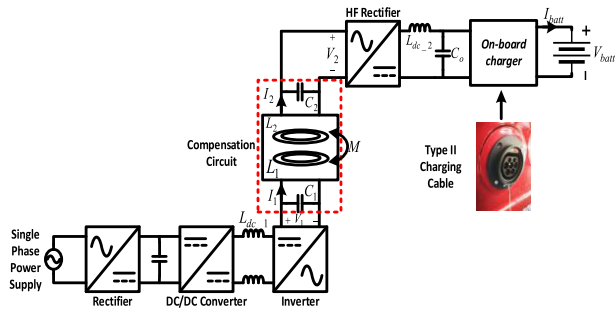
FIGURE 2. Proposed WPT system.

the voltage V_2 at the frequencies ω_0, and ω_2 can be calculated as,

$$V_2(\omega_0)$$
$$= -jV_1 \left(\frac{RC_2 k_{12} \sqrt{L_1 L_2}}{L_1 \sqrt{L_2 C_2 \left(k_{12}^2 - 1\right)}} \right) \tag{16}$$

$$V_2(\omega_2)$$
$$= \frac{V_1 L_2}{2 C_2 k_{12} R^2 \sqrt{L_1 L_2}}$$
$$\times \left(\begin{array}{c} A - L_2 \left(k_{12}^2 - 1\right) \\ +j2\sqrt{2} C_2 L_2 R^2 \left(k_{12}^2 - 1\right) \sqrt{\frac{1}{L_2 \left((k_{12}^2 - 1) L_2 + 2 C_2 R^2 + A\right)}} \end{array} \right) \tag{17}$$

where A is given as,

$$A = \sqrt{\left(k_{12}^2 - 1\right)^2 L_2^2 + 4 C_2 L_2 R^2 \left(k_{12}^2 - 1\right) + 4 C_2^2 k_{12}^2 R^2} \tag{18}$$

The phase difference between V_1 and V_2, at ω_0 in (16), is approximately 90°. As the bifurcation occurs, the ZPA frequency splits into 3 values and the controller tracks for the highest ZPA frequency, namely ω_2. The relationship between V_2 and V_1 at ω_2 becomes (17). Note that the phase difference between V_2 and V_1 is reduced due to the real part in (17). Although the phase difference between V_2 and V_1 indicates the bifurcation, it is not possible to measure the phase of voltage V_2 from the primary side.

III. THE PROPOSED IPT SYSTEM FOR ON-BOARD CHARGER

The block diagram of the proposed IPT system for an on-board charger can be depicted in Figure 2. A single-phase 220Vac power supply is converted to DC source. Both DC-DC converter and the inverter would be used to regulate the primary voltage (V_1) and the inverter current (I_{inv}). Then,

TABLE 2. System specifications.

Parameters	Symbol	Value
Nominal input voltage, 50 Hz	V_{in}	220 V
Output voltage	V_o	275 V
Rated output power	P_o	1000 W
Charging current	I_{batt}	15 A
Battery voltage	V_{batt}	48 V
Load range	R	$78 - 200~\Omega$
Primary inductance of coreless pad	L_1	51 μH
Primary inductance of ferrite pad	L_1	68 μH
Secondary inductance of coreless pad	L_2	51 μH
Secondary inductance of ferrite pad	L_2	68 μH
Primary capacitance	C_1	750 nF
Secondary capacitance	C_2	750 nF
The coupling range	k_{12}	0.15 - 0.24
Sensing coil inductance	L_{sense}	30 μH

the secondary side voltage (V_2) is converted to DC and fed to the on-board charger. The equivalent circuit of rectifier and on-board charger on the secondary side are combined and modelled as the load resistance R.

A. OPERATION REGIONS

Using the parameters in Table 2, Figures 3(a) and 3(b) show the frequency responses of the phase angle of Z_{in} with respect to the coupling k_{12} for coreless and ferrite pads, respectively. When the coupling k_{12} is greater than k_{cri}, bifurcation occurs and the frequency f_0 is split into f_1 and f_2. The recommended operating region is capacitive region (negative phase angle region) for the zero-current-switching (ZCS) condition.

The operable frequency range varies dependently on the coil configuration. For instance, in a coreless pad when $k_{12} = 0.3$, the operable frequency range is from 25.7 kHz to 30.5 kHz. The frequency range becomes smaller as the coil inductances and the coupling increase. To illustrate the constant-voltage gain capability of the proposed method, regardless of coil configuration and coupling coefficient, a ferrite module is added to the coreless pad. Both inductances L_1 and L_2 are increased from 51 μH to 68 μH. The coupling k_{12} is increased from the initial value of 0.22 to 0.24. Consequently, the ZPA frequencies, f_0, f_1 and f_2 are all decreased. Especially, the operating frequency f_2, is reduced from 28.7 kHz to 25.2 kHz. Note that the current frequency range is from 22.3 kHz to 26.3 kHz. Thus, the coverage frequency range when using both ferrite and coreless pads is 22.3 - 30.5 kHz. The operating points when using the coreless and ferrite pads are located on the frequency f_2 trajectory as depicted in Figures 3(a) and 3(b), respectively.
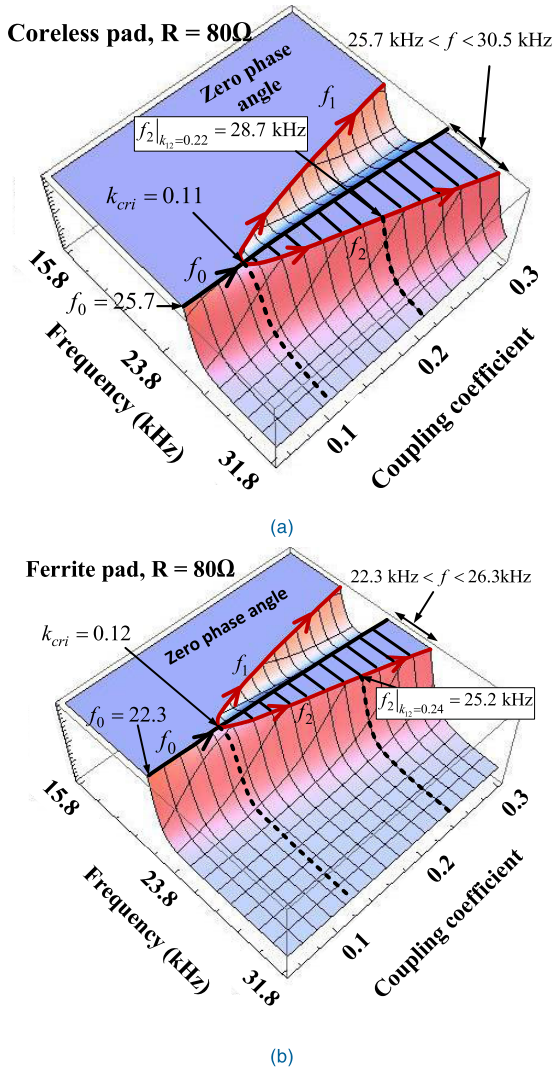
$$V_2(j\omega)$$
$$= \frac{I_{inv} k_{12} L_2 R \sqrt{L_1 L_2} \left(\omega^2 - C_2 L_2 \left(k_{12}^2 - 1\right) \omega^4\right) + j \left(I_{inv} k_{12} R^2 \sqrt{L_1 L_2} \left(\omega - 2 C_2 L_2 \omega^3 + C_2^2 L_2^2 \left(1 - k_{12}^2\right) \omega^5\right)\right)}{R^2 + \left(L_2^2 - 4 C_2 L_2 R^2\right) \omega^2 - 2 C_2 L_2^2 \left(L_2 - k_{12}^2 L_2 - 3 C_2 R^2 + C_2 k_{12}^2 R^2\right) \omega^4 + C_2^2 L_2^2 \left(L_2^2 \left(k_{12}^2 - 1\right)^2 + 4 C_2 L_2 R^2 \left(k_{12}^2 - 1\right)\right) \omega^6 + R^2 C_2^4 L_2^4 \left(k_{12}^2 - 1\right)^2 \omega^8} \tag{15}$$

FIGURE 3. Frequency responses of input phase angle with respect to coupling coefficient, (a) coreless and (b) ferrite pad configurations.

B. COUPLING INDEPENDENT OPERATION

Since the coupling coefficient k_{12} no longer has effect on the input impedance at ω_1 and ω_2. This means that both input voltage and current remain constant for virtually any coil distance and misalignment. The secondary voltage V_2 is shown in (15). Referring to (10), the magnitude of voltage V_2 at the ZPA frequency ω_2 can be found as,

$$|V_2|_{\omega=\omega_2} = I_{inv}R\sqrt{\frac{L_1}{L_2}} \qquad (19)$$

Clearly, the voltage V_2 is independent of the coupling. The system now possesses a flexible charging position capability with constant voltage for a given load resistance R. The voltage gain (G_v) and current gain (G_I) can be given as,

$$|G_v(\omega_2)| = \sqrt{\frac{L_2}{L_1}} \qquad (20)$$

$$|G_I(\omega)| = \frac{1}{|G_v(\omega)|} \qquad (21)$$
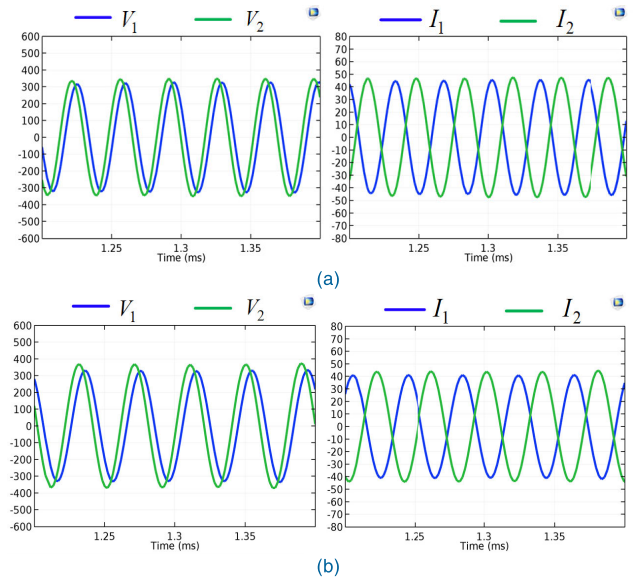
FIGURE 4. FEM waveform results for $R = 80\ \Omega$ and airgap $= 15$ cm, (left) V_1 vs V_2, (right) I_1 vs I_2, (a) coreless and (b) ferrite pad configurations.

Referring to (20) and (21), both voltage and current gains are independent on the coupling coefficient k_{12} as long as the bifurcated condition is maintained. To illustrate the coupling independence on the magnetic domain, different coil configurations, namely the coreless and ferrite pads are simulated using COMSOL multiphysics software package [20]. Simulation studies using finite element method (FEM) are performed basing on system parameters given in Table 2.

To verify the independently coupling operation, the inclusion of ferrites essentially changes the coil configuration by increasing the inductances from 51 to 68 μH. The coupling coefficient k_{12} is increased from 0.22 to 0.24, corresponding to the operating frequencies f_2 of 28.7 and 25.2 kHz, respectively. Note that in both cases, the system is intentionally operated under bifurcation. Since the primary and secondary coils assume the same geometry ($L_1 = L_2$), the unity gain operation, as in (20) and (21), is possible. As shown in Figure 4, the magnitudes of the primary voltage V_1 and current I_1 are similar to the secondary voltage V_2 and current I_2. The difference in the current magnitude is at 6% while the difference in voltage magnitude is slightly larger at 10%. The maximum flux density on the coupling coils without ferrite in Figure 5 is at 3.5 mT, and it is increased to 4.4 mT as the ferrites are included.

C. BIFURCATION DETECTION USING SENSING COIL

The bifurcation detection serves as a safety measure to ensure that the system never operates under misalignment and load condition mismatch beyond the design boundaries. The bifurcation condition must be ensured before the system is initiated.

A sensing coil (L_{sense}) for bifurcation detection in an IPT system is proposed, as shown in Figure 6. The sensing coil is placed in the middle between the primary and secondary
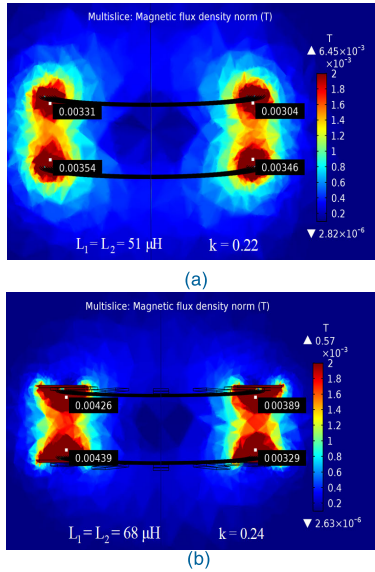
FIGURE 5. Magnetic flux density distribution results, (a) coreless and (b) ferrite pad configurations.
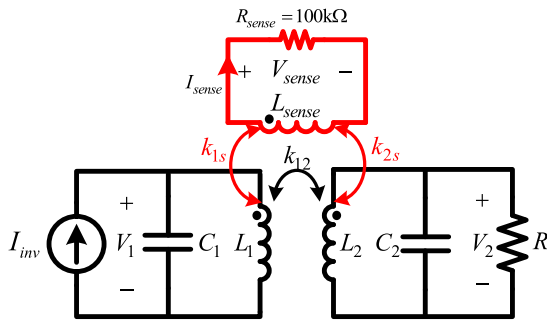

FIGURE 6. Equivalent circuit of the PP system with bifurcation sensing circuit.

coils. The main purpose of the sensing coil is to detect the leakage flux as a result of the phase difference between V_2 and V_1 (θ_{v1-2}), which can be used as a bifurcation indicator. The coupling between L_1 and L_{sense} is represented by k_{1s}. Similarly, k_{2s} is the coupling between L_2 and L_{sense}. The voltage and current relationships on the primary, secondary, and sensing circuits are given below,

$$I_{in}(j\omega) = \left(j\omega C_1 + \frac{1}{j\omega L_1}\right)V_1 - \frac{k_{12}\sqrt{L_1 L_2}}{L_1}I_2$$
$$- \frac{k_{1s}\sqrt{L_1 L_{sense}}}{L_1}I_{sense} \qquad (22)$$

$$0 = -\frac{k_{12}\sqrt{L_1 L_2}}{L_2}I_1 - \frac{k_{2s}\sqrt{L_2 L_{sense}}}{L_2}I_{sense}$$
$$+ \left(\frac{1}{j\omega L_2} + j\omega C_2 + \frac{1}{R}\right)V_2 \qquad (23)$$

$$V_{sense}(j\omega) = j\omega L_{sense}I_{sense} - j\omega k_{1s}\sqrt{L_1 L_3}I_1$$
$$- j\omega k_{2s}\sqrt{L_2 L_{sense}}I_2 \qquad (24)$$

To minimize interferences due to the current I_{sense} on the primary and secondary coils, the following conditions are assumed:
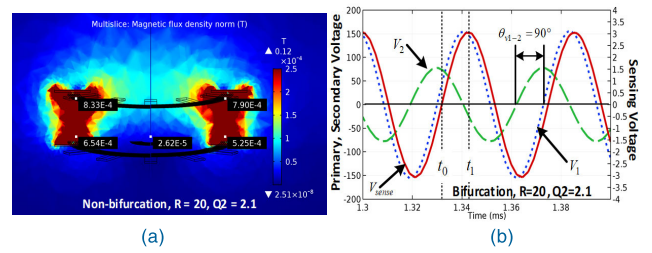

FIGURE 7. Non-bifurcated operation with $R = 20\ \Omega$, $Q_2 = 2.1$, (a) magnetic flux density and (b) main and sensing coil voltage waveforms.
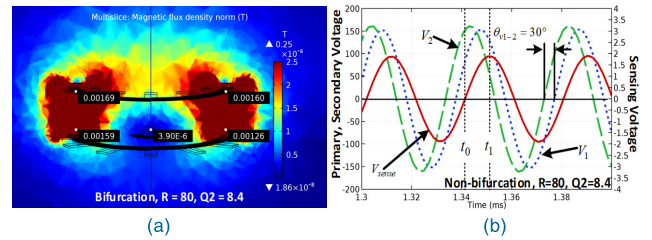

FIGURE 8. Bifurcated operation with $R = 80\ \Omega$, $Q_2 = 8.4$, (a) magnetic flux density and (b) main and sensing coil voltage waveforms.

- The k_{1s} and k_{2s} are negligible compared with the coupling between the main coils (k_{12}).
- The sensing resistor (R_{sense}) is sufficiently high to avoid interference emanated by the sensing current (I_{sense}).

The simplified sensing voltage, V_{sense}, can be formulated as,

$$V_{sense}(j\omega) = -\frac{k_{1s}\sqrt{L_1 L_{sense}}}{L_1}V_1$$
$$- j\omega\sqrt{L_2 L_{sense}}\left(k_{12}k_{1s} - k_{2s}\right)\left(\frac{Q_2}{R}\right)V_2 \qquad (25)$$

The difference between the voltages V_1 and V_2 is related to the leakage flux and the induced voltage on the sensing coil. The primary side is operated at the highest possible ZPA frequency. The voltage V_1 is constant regardless of the coupling k_{12} and load resistance R. Finite element simulation results for operations under non-bifurcation with $R = 20\ \Omega$ and bifurcation with $R = 80\ \Omega$ are shown in Figures 7 and 8, respectively. The voltage V_1 and coupling k_{12} are kept constant in both cases.

For the case of non-bifurcated condition in Figure 7, at t_1 while V_{sense} is at the peak value, the maximum magnetic flux density measured at the primary ($B_{primary}$) and sensing (B_{sense}) coils are 0.654 mT and 26.2 μT, respectively, as illustrated in Figure 7(a). The voltage V_2 in Figure 7(b) is 50% less than V_1, while the phase angle θ_{v1-2} is at 90°. The voltage V_{sense} induced by the leakage flux from the main coils is around 1.93 % of voltage V_1. On the other hand, under bifurcation, R is equal to 80 Ω. The flux linkage is increased. The voltage V_2 also increases and becomes slightly larger than V_1. The leakage flux on the sensing coil B_{sense} is reduced to 3.9 μT, as shown in Figure 8(a). A very low leakage flux is a result of the phase θ_{v1-2} reduction to 30°. The voltage V_{sense} is reduced to 1.2% of the voltage V_1 as shown
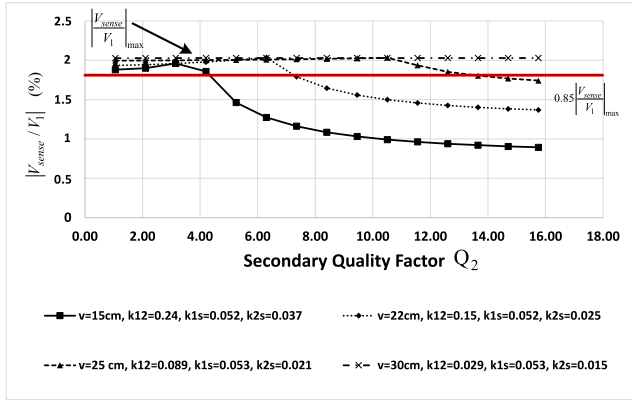
FIGURE 9. V_{sense} vs. Q_2 under various coupling conditions.

in Figure 8(b). Since V_{sense} greatly varies from one value under the bifurcation operation to another value under non-bifurcation, therefore it can serve as the bifurcation indicator.

The critical coupling k_{cri} is commonly formulated as a function of Q_2 as mentioned in Table 1. Figure 9 shows the relations of voltage V_{sense} vs Q_2 under various values of coupling k_{12} obtained from the FEM studies. The ratio between V_{sense} and V_1 (V_{sense}/V_1) is increased as the vertical distance increases. When the coupling k_{12} approaches zero, the voltage V_{sense} is at its maximum and remains constant regardless of Q_2. Once the bifurcation occurs, the ratio V_{sense}/V_1 noticeably decreases.

According to (25), the maximum sensing voltage can be estimated as,

$$\left| \frac{V_{sense}}{V_1} \right|_{\max} = \frac{k_{1s}\sqrt{L_1 L_{sense}}}{L_1} \qquad (26)$$

Normally, the coupling k_{12} for EV application is in the range of $0.15 \sim 0.24$. The operating condition under the vertical distance of 15 cm and Q_2 of 1 in Figure 9 yields 85% of the ratio V_{sense}/V_1 in (26). It is empirically chosen as the bifurcation boundary.

D. PROPOSED CONTROL
An implementation of the secondary voltage control based on the primary-side controller is demonstrated in Figure 10. The proposed controller consists of two parts as follows.

1) PHASE-LOCKED-LOOP CONTROL
The PLL controller regulates the input impedance phase angle, which is the phase difference between the current I_{inv} and voltage V_1. As shown in Figure 10, the impedance phase angle is detected by the zero-crossing detector (ZCD) through the phase detector module inside 4046 IC chip. The phase angle is converted to a DC value via the low-pass filter (LPF). The PI controller modifies the phase angle response. The switching frequency (f_s) is maintained above the highest possible ZPA frequency.

Initially, the switching frequency (f_s) is set at the maximum frequency ($f_{\max}$). The controller then reduces f_s until the impedance angle is within the setting value. f_s is maintained
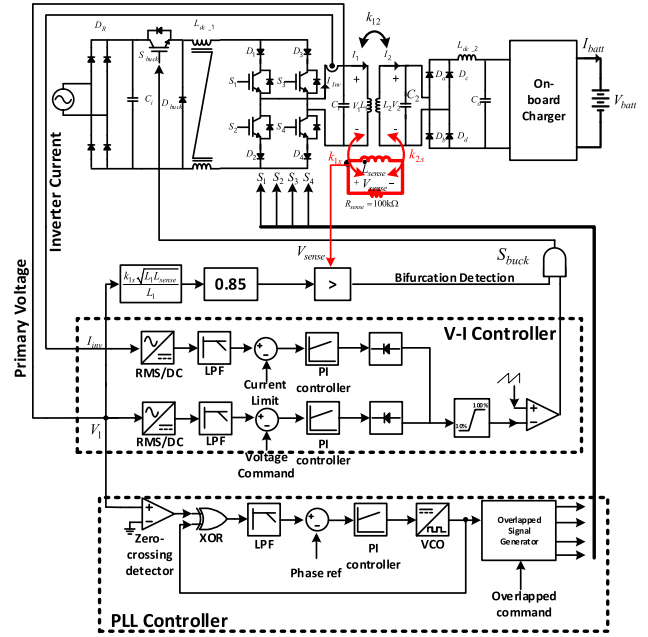

FIGURE 10. Secondary voltage controller based on primary side control with bifurcation detection.

slightly higher than the targeted ZPA frequency for the desired phase angle. When the bifurcation is occurred, the constant voltage gain operation is possible by tracking the frequency f_2. The duty cycle of driving signals in inverter is set to 54 % for overlapping period of the CSI.

2) V-I CONTROLLER
Since the inverter operates at the frequency f_2 by PLL controller, the voltage V_2 is directly controlled by the voltage V_1 regardless of load and coupling variations as referred in (20). The V-I controller consists of voltage-control and current-limit loops using conventional PI controller. The voltage V_1 is regulated, while the inverter current I_{inv} depends on load requirements. The secondary voltage V_2 is regulated through the voltage V_1 in the voltage control loop. The current limit of I_{inv} is implemented through the current control loop. Note that V-I controller is enabled by the bifurcation detection loop as mentioned in the previous section.

IV. DESIGN
A. LOAD MODEL
The on-board charger in Figure 2 receives electrical power from the PP compensation and regulates the charging current (I_{batt}) and battery voltage (V_{batt}). The charging process consists of two stages, constant current (CC) charging mode and constant voltage (CV) charging mode. The ac equivalent load resistance seen by secondary side is given by [21].

$$R = \frac{\pi^2}{8} \left(\frac{\eta_{\text{charger}} V_o^2}{V_{batt} I_{batt}} \right) \qquad (27)$$

The charging profile of the on-board battery charger with 80% of efficiency is shown in Figure 11. The following load
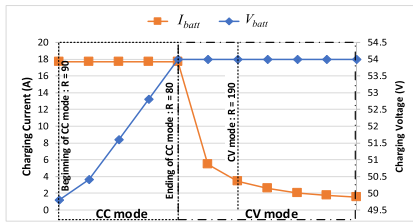
FIGURE 11. The charging profile of 6 cells of 3K T-885 lead acid battery.

FIGURE 12. Primary, secondary, and sensing coil details.

FIGURE 13. The coupling coefficient k_{12} plot for the different value of misalignment.

conditions are considered as a representative of each mode of operation.

1) CC MODE

Initially, the charging process begins with the CC mode, as shown in Figure 11. The on-board charger behaves as a resistive load with the equivalent resistance of 90 Ω. The current I_{batt} is regulated at 17.8 A. At the end of this stage, the V_{batt} reaches 54 V. The equivalent load resistance is reduced to 80 Ω and the supplied power is at its maximum.

2) CV MODE

In this mode the output voltage is regulated. As the equivalent resistance is increased, the charging current reduces. Experimental waveforms of the case when the equivalent resistance is at 190 Ω are considered.

B. DESIRED COIL INDUCTANCE CALCULATION

From the relationship in (11), the maximum secondary inductance L_2 under bifurcation condition can be calculated as,

$$L_2 < \frac{2\left(C_2R^2 - C_2k_{12}^2R^2 - \sqrt{C_2^2R^4 - 3C_2^2k_{12}^2R^4 - C_2^2R^4k_{12}^6}\right)}{\left(k_{12}^2 - 1\right)^2}$$

(28)

Note that the primary inductance L_1 is selected by the voltage gain in (20) and the primary capacitance C_1 calculated in (6). The circular coil is often chosen for static wireless charging application, because the symmetrical configuration allows the secondary coil movement from any directions. The primary and secondary coils are made of 7 turns of 600 strands of SWG39 wire. The ferrite bars are included for magnetic flux shielding and guiding. The dimension of I-core ferrite bars is $120 \times 40 \times 6$ mm.

C. MISALIGNMENT CONSIDERATION

For the desired load values of 80 ∼ 190 Ω, the L_1 and L_2 inductances are both at 68 μH while the critical coupling k_{cri} is at 0.12. The relationships between the coupling coefficient k_{12} and the lateral misalignment at different vertical distance is shown in Figure 13. The coupling coefficient reduces as the misalignment is increased. So long as the coupling coefficient is greater than the critical coupling ($k_{12} > k_{cri}$), the coupling independent operation is possible. In this work, the k_{cri} allows
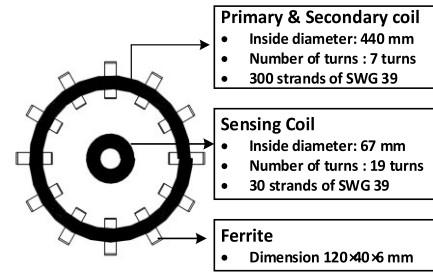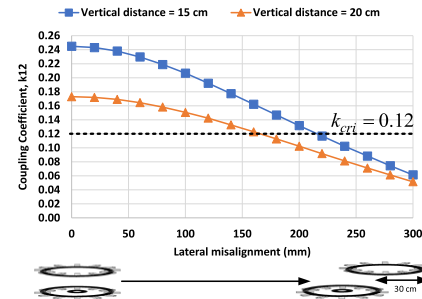
the misalignment up to 16 cm and 22 cm at the vertical distances of 20 cm and 15 cm, respectively.

V. EXPERIMENTAL RESULTS

A 1-kW IPT hardware prototype with the proposed control is implemented in a golf cart as shown in Figure 14(a). The system parameters are given in Table 2. The primary side consists of a buck converter and a full-bridge current-source inverter supplying the square-wave current I_{inv} to the PP compensation circuit. The converter and inverter are constructed by using IRGPH40UD IGBTs. To block negative voltage on the switches, RURG 8060 fast recovery diodes are connected in series with the IGBTs. The RURG 8060 diodes are also used in the rectifier circuit on the secondary side. The vertical distance for the experimental study is 15 cm with the coupling between main coils k_{12} at 0.24. The relative position of the primary, secondary, and sensing coil is shown in Figure 14(b).

A. OPERATION UNDER COUPLING INDEPENDENT

An experimental study is conducted to demonstrate the impact of the proposed bifurcation control and operation under coupling independent, through a sudden misalignment. As shown in Figure 15, the coils are initially in perfect alignment (cursor position 1), where both V_1 and V_2 are at 100 V. The operating frequency is at 25.2 kHz, while the inverter and load currents are both at 1 A. Then, the secondary coil is abruptly moved to the position of 20-cm misalignment. The coupling is reduced from 0.24 to 0.13. In Figure 3, the PLL controller continues to track the ZPA frequency f_2 and automatically reduces the operating frequency to 23.1 kHz. The voltages and currents remain the same, as shown at cursor position 2. Clearly, with the proposed control, both voltage
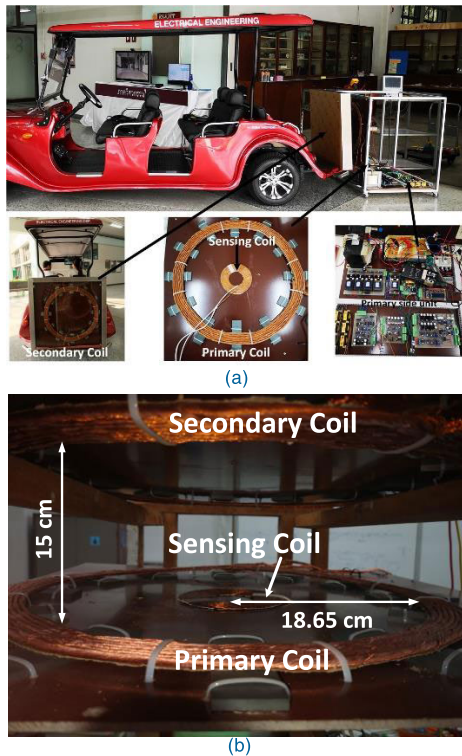
(a)

(b)

FIGURE 14. Experimental setup for (a) the golf cart, (b) the relative position of primary, secondary, and sensing coils.
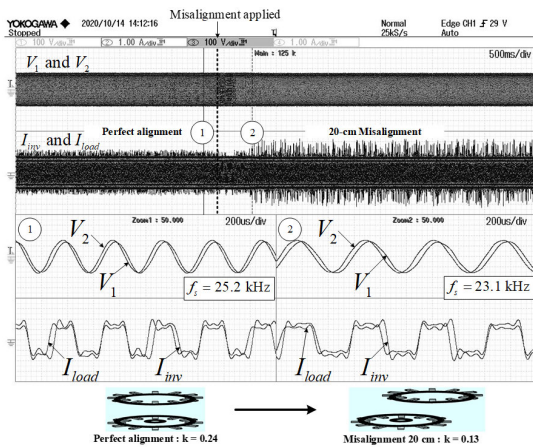

FIGURE 15. Experimental results under abrupt misalignment, (top to bottom) V_1, V_2, I_{inv}, and I_{load}, under perfect alignment (cursor position 1) and 20-cm misalignment (cursur position 2).

and current are regulated regardless of the misalignment, provided that the system is operated under bifurcation.

B. BIFURCATION DETECTION

At the vertical distance of 15 cm, the coupling k_{1s} and k_{2s} is at 0.053 and 0.037, respectively. The load quality factor Q_2 is set at 2. The bifurcation boundary in (26) is selected as 85% which is equal to the ratio V_{sense}/V_1 at 1.8 %. Figure 16(a) shows the waveform measurement under non-bifurcated condition, the same condition as in Figure 7. The inverter is operated at f_0 which is 23.33 kHz. The phase angle θ_{v1-2}
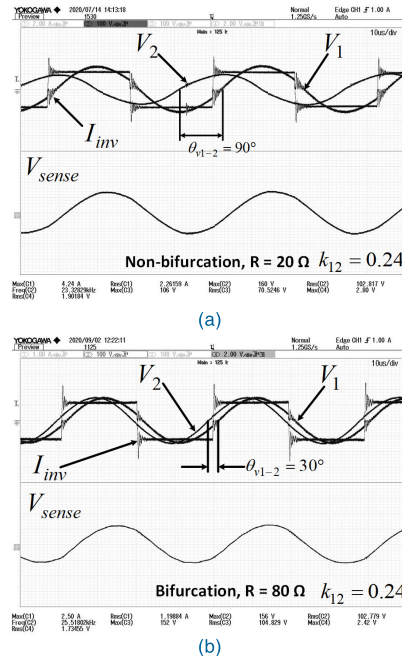

(a)

(b)

FIGURE 16. Measured waveforms for bifurcation detection of I_{inv}, V_1, V_2 and V_{sense} under (a) non-bifurcation and (b) bifurcation conditions.

is at 90° as mentioned in (16) and the voltage V_2 is lower than V_1. The voltages V_{sense} and V_1 are at 1.9 V and 103V, respectively. The ratio V_{sense}/V_1 is 1.85%, which is greater than the bifurcation boundary. This indicates that the system is operated under non-bifurcated condition.

The measured waveforms for the bifurcated condition are shown in Figure 16(b). For comparison purpose, the voltage V_1 is kept constant at 103 V. When the quality factor Q_2 is increased to 8, the voltage V_2 also increases to 108 V. The unity voltage gain is achieved, since the frequency increases to 25.42 kHz which is slightly higher than the frequency f_2. The phase θ_{v1-2} is now at 30° as mentioned in (17). The ratio V_{sense}/V_1 is reduced to 0.85 %, which is lower than the bifurcation boundary. This confirms the operation under bifurcation. Clearly, the bifurcation detection is possible through the proposed ratio V_{sense}/V_1 and the corresponding boundary.

C. OPERATION UNDER CHARGING CONDITIONS

The waveforms during start-up of the on-board charger are shown in Figure 17. The system is initiated by applying 280 V of the voltage V_1. After the voltage V_2 reaches the desired value, the on-board charger then supplies a constant current I_{batt} at 15 A to the battery pack while the current I_{inv} is at 4.5 A. The voltage V_{batt} is at 54 V. Note that the voltage V_1 remains rather constant even though the load current is changed from 0 A to 15 A.

Figure 18(a) shows the measured waveforms during the beginning of CC mode. The switching frequency f_s is at 25.4 kHz. The voltage V_2 of 284.2 V and current I_{load} of 3.2 A are obtained under steady state. The output power P_{out} is at 815 W. Measured waveforms on the battery side are shown in Figure 18(b). The voltage V_{batt} is at 47.4 V while the
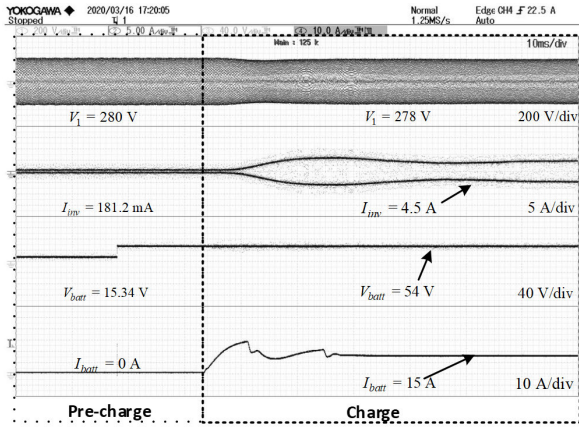
FIGURE 17. Measured waveforms during start-up of on-board charger. (top to bottom) V_1, I_{inv}, V_{batt}, and I_{batt}.
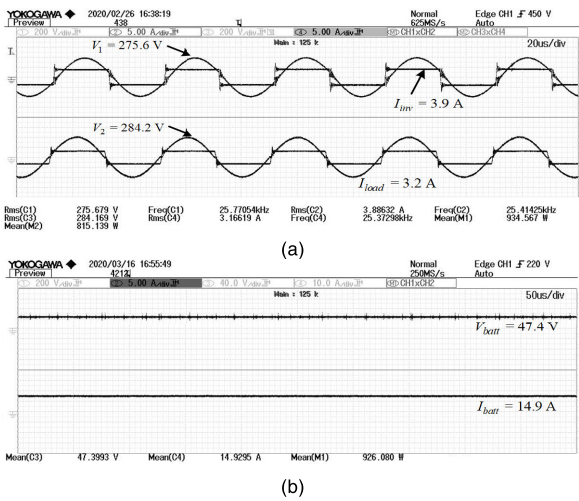

FIGURE 18. Measured waveforms at the beginning of CC mode. (a) V_1, I_{inv}, V_2, and I_{load}, and (b) V_{batt} and I_{batt}.

FIGURE 19. Measured waveforms at the end of CC mode. (a) V_1, I_{inv}, V_2 and I_{load}, and (b) V_{batt} and I_{batt}.

FIGURE 20. Measured waveforms during CV mode. (a) V_1, I_{inv}, V_2 and I_{load}, and (b) V_{batt} and I_{batt}.

battery is charged under constant charging current I_{batt} at 14.9 A. When the battery voltage is close to the desired value, the voltage V_2 remains at 284.8 V, as shown in Figure 19(a). The current I_{load} increases to 3.6 A and the equivalent resistance in (27) is reduced. The switching frequency f_s is reduced to track the frequency f_2 at 25.3 kHz. The output power P_{out} is also increased to 931.5 W. The voltage V_{batt} is at 54 V and the current I_{batt} is constant at 14.9 A as illustrated in Figure 19(b).

The waveforms of an operation under CV mode are shown in Figure 20(a). The voltage V_2 is at 287 V following the voltage V_1 at 274 V. The current I_{batt} is reduced to 1.5 A. As a result, the voltage V_{batt} is maintained at 54 V while the current I_{batt} is decreased to 3.3 A as depicted in Figure 20(b).

D. PRACTICAL OPERATION IN THE COUPLING VARIATION

Figure 21 describes the primary, secondary, and sensing coil voltage characteristics with respect to the coil coupling. The primary voltage V_1 is kept constant to avoid unnecessary interaction. When the coupling is less than k_{cri}, the secondary voltage V_2 varies with the coupling, while the ZPA
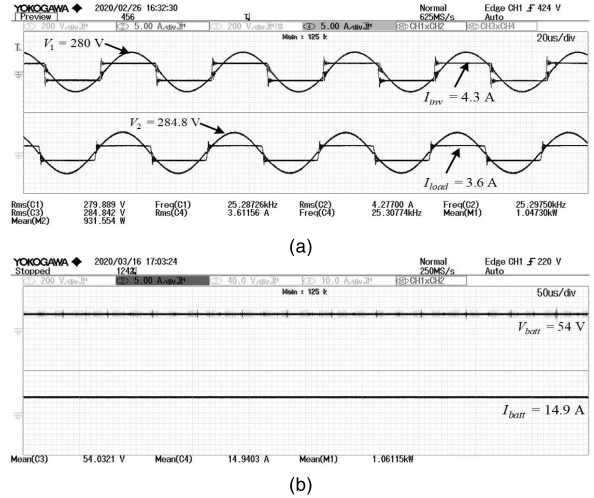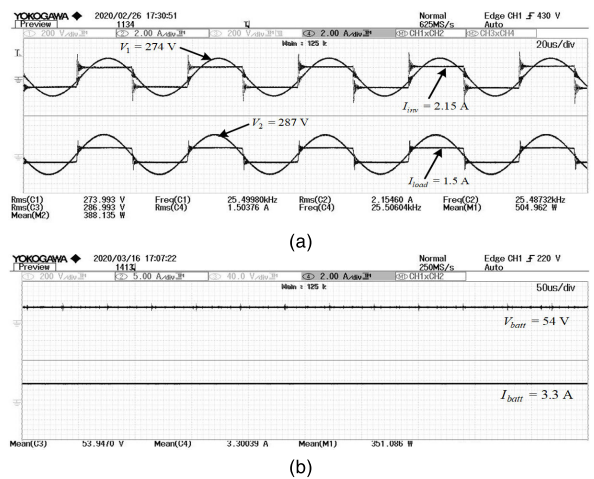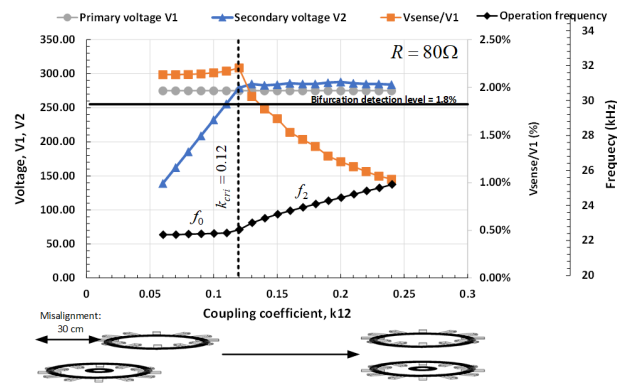

FIGURE 21. Voltage and frequency characteristics of the secondary voltage controller, PLL controller and bifurcation detection under coupling variations.

frequency is constant. As the coupling becomes greater than k_{cri}, bifurcation occurs and V_2 remains constant regardless of the coupling value. At the same time, V_{sense} is reduced
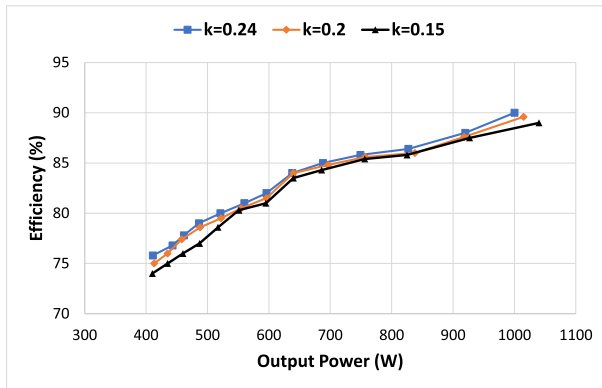
FIGURE 22. Efficiency vs. output power.

whereas the ZPA frequency f_2 is increased. The rate of change of the ratio V_{sense}/V_1 can be used to identify the bifurcation. Clearly, the ratio V_{sense}/V_1 reduces noticeably under bifurcation. However, the detection level is selected with a desired margin to guarantee bifurcated operation. The bifurcation detection level is set at 1.8%.

E. EFFICIENCY

The system efficiency is obtained throughout the operation as illustrated in Figure 22. The output power and efficiency of the proposed system are plotted for three different coupling conditions at $k_{12} = 0.24$, 0.20, and 0.15 corresponding to the vertical distances of 15 cm, 20 cm, and 25 cm, respectively. Note that within a given load condition, the output power remains relatively the same even when the coupling coefficient k_{12} is varied. The maximum efficiency of the proposed wireless charger system can be accomplished up to 90% for the rated power of 1 kW. The efficiency is decreased as the output power decreases. Overall, the effect of coil position on the implemented system is insignificant.

VI. CONCLUSION

In this article, the wireless power supply for on-board charger has been proposed. By approaching bifurcation, the proposed secondary-voltage controller based on primary-side control offers constant-voltage gain feature under a variety of loads and coupling coefficients. Moreover, the bifurcation detection is performed via the sensing coil located in the middle of the primary coil. The constant voltage gain can be achieved in both coreless power pad and the pad with ferrites providing a flexibility of coupling coefficient and inductance variations. With the proposed method, cores made of ferromagnetic material could be reduced or even removed for the benefit of size, weight, and cost. Experimental results confirm that the proposed system is suitable for the on-board charger with the maximum efficiency of 90%.

REFERENCES

[1] D. Patil, M. K. McDonough, J. M. Miller, B. Fahimi, and P. T. Balsara, "Wireless power transfer for vehicular applications: Overview and challenges," *IEEE Trans. Transport. Electrific.*, vol. 4, no. 1, pp. 3–37, Mar. 2018.

[2] C.-S. Wang, G. A. Covic, and O. H. Stielau, "Power transfer capability and bifurcation phenomena of loosely coupled inductive power transfer systems," *IEEE Trans. Ind. Electron.*, vol. 51, no. 1, pp. 148–157, Feb. 2004.

[3] Z. Zhang, H. Pang, A. Georgiadis, and C. Cecati, "Wireless power transfer—An overview," *IEEE Trans. Ind. Electron.*, vol. 66, no. 2, pp. 1044–1058, Feb. 2019.

[4] S. Chudjuarjeen, A. Sangswang, and C. Koompai, "An improved *LLC* resonant inverter for induction-heating applications with asymmetrical control," *IEEE Trans. Ind. Electron.*, vol. 58, no. 7, pp. 2915–2925, Jul. 2011.

[5] A. Berger, M. Agostinelli, S. Vesti, J. A. Oliver, J. A. Cobos, and M. Huemer, "A wireless charging system applying phase-shift and amplitude control to maximize efficiency and extractable power," *IEEE Trans. Power Electron.*, vol. 30, no. 11, pp. 6338–6348, Nov. 2015.

[6] B. X. Nguyen, D. M. Vilathgamuwa, G. H. B. Foo, P. Wang, A. Ong, U. K. Madawala, and T. D. Nguyen, "An efficiency optimization scheme for bidirectional inductive power transfer systems," *IEEE Trans. Power Electron.*, vol. 30, no. 11, pp. 6310–6319, Nov. 2015.

[7] J. Liu, K. W. Chan, C. Y. Chung, N. H. L. Chan, M. Liu, and W. Xu, "Single-stage Wireless-Power-Transfer resonant converter with boost bridgeless Power-Factor-Correction rectifier," *IEEE Trans. Ind. Electron.*, vol. 65, no. 3, pp. 2145–2155, Mar. 2018.

[8] T. Diekhans and R. W. De Doncker, "A dual-side controlled inductive power transfer system optimized for large coupling factor variations and partial load," *IEEE Trans. Power Electron.*, vol. 30, no. 11, pp. 6320–6328, Nov. 2015.

[9] T. Mishima and E. Morita, "High-frequency bridgeless rectifier based ZVS multiresonant converter for inductive power transfer featuring high-voltage GaN-HFET," *IEEE Trans. Ind. Electron.*, vol. 64, no. 11, pp. 9155–9164, Nov. 2017.

[10] N. Hatchavanich, M. Konghirun, and A. Saengswang, "The analysis of series—Parallel—Parallel compensation current source inverter for wireless power transfer in EVs charging application," in *Proc. IEEE 12th Int. Conf. Power Electron. Drive Syst. (PEDS)*, Honolulu, HI, USA, Dec. 2017, pp. 1–093.

[11] E. Gati, G. Kampitsis, and S. Manias, "Variable frequency controller for inductive power transfer in dynamic conditions," *IEEE Trans. Power Electron.*, vol. 32, no. 2, pp. 1684–1696, Feb. 2017.

[12] Y. Zhang and Z. Zhao, "Frequency splitting analysis of two-coil resonant wireless power transfer," *IEEE Antennas Wireless Propag. Lett.*, vol. 13, pp. 400–402, 2014.

[13] S. Moon, B.-C. Kim, S.-Y. Cho, C.-H. Ahn, and G.-W. Moon, "Analysis and design of a wireless power transfer system with an intermediate coil for high efficiency," *IEEE Trans. Ind. Electron.*, vol. 61, no. 11, pp. 5861–5870, Nov. 2014.

[14] S. Moon and G.-W. Moon, "Wireless power transfer system with an asymmetric four-coil resonator for electric vehicle battery chargers," *IEEE Trans. Power Electron.*, vol. 31, no. 10, pp. 6844–6854, Oct. 2016.

[15] A. P. Sample, D. A. Meyer, and J. R. Smith, "Analysis, experimental results, and range adaptation of magnetically coupled resonators for wireless power transfer," *IEEE Trans. Ind. Electron.*, vol. 58, no. 2, pp. 544–554, Feb. 2011.

[16] R. Huang and B. Zhang, "Frequency, impedance characteristics and HF converters of two-coil and four-coil wireless power transfer," *IEEE J. Emerg. Sel. Topics Power Electron.*, vol. 3, no. 1, pp. 177–183, Mar. 2015.

[17] F. Mastri, A. Costanzo, and M. Mongiardo, "Coupling-independent wireless power transfer," *IEEE Microw. Wireless Compon. Lett.*, vol. 26, no. 3, pp. 222–224, Mar. 2016.

[18] M. Kosik, R. Fajtl, and J. Lettl, "Analysis of bifurcation in two-coil inductive power transfer," in *Proc. IEEE 18th Workshop Control Model. for Power Electron. (COMPEL)*, Stanford, CA, USA, Jul. 2017, pp. 1–8.

[19] K. Aditya and S. S. Williamson, "Design guidelines to avoid bifurcation in a Series–Series compensated inductive power transfer system," *IEEE Trans. Ind. Electron.*, vol. 66, no. 5, pp. 3973–3982, May 2019.

[20] (2019). *Comsol Multiphysics, Comsol.* Accessed: Aug. 22, 2019. [Online]. Available: https://www.comsol.com/support

[21] M. T. Outeiro, G. Buja, and D. Czarkowski, "Resonant power converters: An overview with multiple elements in the resonant tank network," *IEEE Ind. Electron. Mag.*, vol. 10, no. 2, pp. 21–45, Jun. 2016.

[22] E. Gati, G. Kampitsis, L. Stavropoulos, S. Papathanassiou, and S. Manias, "Wireless phase-locked loop control for inductive power transfer systems," in *Proc. IEEE Appl. Power Electron. Conf. Expo. (APEC)*, Charlotte, NC, USA, 2015, pp. 1601–1607.

[23] X. Liu, C. Liu, and P. W. T. Pong, "TMR-Sensor-Array-Based misalignment-tolerant wireless charging technique for roadway electric vehicles," *IEEE Trans. Magn.*, vol. 55, no. 7, pp. 1–7, Jul. 2019.

[24] X. Liu, C. Liu, W. Han, and P. W. T. Pong, "Design and implementation of a multi-purpose TMR sensor matrix for wireless electric vehicle charging," *IEEE Sensors J.*, vol. 19, no. 5, pp. 1683–1692, Mar. 2019.

[25] I. Cortes and W.-J. Kim, "Lateral position error reduction using misalignment-sensing coils in inductive power transfer systems," *IEEE/ASME Trans. Mechatronics*, vol. 23, no. 2, pp. 875–882, Apr. 2018.

ANAWACH SANGSWANG (Member, IEEE) was born in Bangkok, Thailand. He received the B.Eng. degree from the King Mongkut's University of Technology Thonburi (KMUTT), Bangkok, in 1995, and the M.S. and Ph.D. degrees in electrical engineering from Drexel University, Philadelphia, PA, USA, in 1999 and 2003, respectively.

From 1999 to 2003, he was a Research Assistant with the Center for Electric Power Engineering, Drexel University. Since 2006, he has been an Assistant Professor with the Department of Electrical Engineering, KMUTT. His research interests include induction heating, wireless power transfer, energy management systems, and power system stability.

NATTAPONG HATCHAVANICH (Member, IEEE) received the B.Eng. degree in electrical engineering from the King Mongkut's University of Technology North Bangkok (KMUTNB), Bangkok, in 2012, and the M.Eng. degree in electrical engineering and the D.E. degree in electrical and information engineering technology from the King Mongkut's University of Technology Thonburi (KMUTT), Bangkok, in 2016 and 2020, respectively. His current research interests include the resonant inverter and control technique for wireless power transfer system (WPT) and induction heating applications.

MONGKOL KONGHIRUN (Senior Member, IEEE) received the B.Eng. degree (Hons.) in electrical engineering from the King Mongkut's University of Technology Thonburi, Bangkok, Thailand, in 1995, and the M.Sc. and Ph.D. degrees in electrical engineering from The Ohio State University, Columbus, OH, USA, in 1999 and 2003, respectively. He is currently an Associate Professor with the Department of Electrical Engineering, King Mongkut's University of Technology Thonburi. His research interests include electric motor drives, power electronics, railway electrification, and renewable energy.

• • •